Article

# Fast Organic Cation Exchange in Colloidal Perovskite Quantum Dots toward Functional Optoelectronic Applications

Chenyu Zhao, Claudio Cazorla, Xuliang Zhang, Hehe Huang, Xinyu Zhao, Du Li, Junwei Shi, Qian Zhao, Wanli Ma, and Jianyu Yuan*

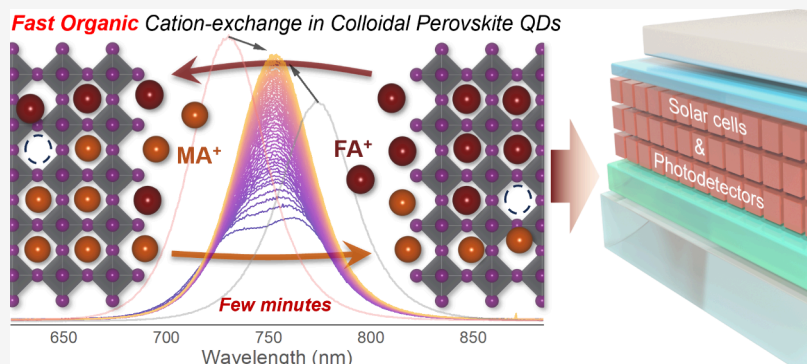Cite This: *J. Am. Chem. Soc.* 2024, 146, 4913−4921

Read Online

ACCESS | Metrics & More | Article Recommendations | SI Supporting Information



Fast Organic Cation-exchange in Colloidal Perovskite QDs

**ABSTRACT:** Colloidal quantum dots with lower surface ligand density are desired for preparing the active layer for photovoltaic, lighting, and other potential optoelectronic applications. In emerging perovskite quantum dots (PQDs), the diffusion of cations is thought to have a high energy barrier, relative to that of halide anions. Herein, we investigate the fast cross cation exchange approach in colloidal lead triiodide PQDs containing methylammonium (MA$^+$) and formamidinium (FA$^+$) organic cations, which exhibits a significantly lower exchange barrier than inorganic cesium (Cs$^+$)-FA$^+$ and Cs$^+$-MA$^+$ systems. First-principles calculations further suggest that the fast internal cation diffusion arises due to a lowering in structural distortions and the consequent decline in attractive cation−cation and cation−anion interactions in the presence of organic cation vacancies in mixed MA$^+$-FA$^+$ PQDs. Combining both experimental and theoretical evidence, we propose a vacancy-assisted exchange model to understand the impact of structural features and intermolecular interaction in PQDs with fewer surface ligands. Finally, for a realistic outcome, the as-prepared mixed-cation PQDs display better photostability and can be directly applied for one-step coated photovoltaic and photodetector devices, achieving a high photovoltaic efficiency of 15.05% using MA$_{0.5}$FA$_{0.5}$PbI$_3$ PQDs and more precisely tunable detective spectral response from visible to near-infrared regions.

## INTRODUCTION

Lead halide perovskites are not only poised to be tremendously important for photovoltaics but also to be disruptive in the field of colloidal quantum dots.[1−3] The emerging perovskite quantum dots (PQDs) offer expanded compositional modulation and surface manipulation capabilities over their bulk counterpart.[4−7] Apart from their high surface-to-volume ratio, the more ionic nature of halide PQDs is beneficial for the postsynthetic management of chemical compositions.[8,9] Postsynthetic ion exchange not only preserves the overall size and shape but also allows for compositionally tunable materials.[10−12] The anion exchange is more efficient and versatile,[13−15] while the rigid cationic sublattice increases the difficulty of cation exchange transformations in PQDs.[16,17] Quite recently, ligand-assisted A-site cation exchange has been explored[18] and demonstrated to be extremely important in terms of functional optoelectronic applications.[19−21]

Through targeted substitutions within the perovskite lattice, cation exchange allows the synthesis of mixed A-site cation PQDs with tailored properties, enhancing the performance of PQD-based optoelectronic devices.[22−25] For instance, mixed Cs$_{1−X}$MA$_X$PbI$_3$ PQDs (Cs = cesium, MA = methylammonium) exhibit the ability to surmount the phase transition from the γ-phase to the δ-phase observed in CsPbI$_3$ as well as the degradation of MAPbI$_3$ to lead iodide, preserving improved structural and thermal stability.[26] In addition, the integration of mixed Cs$_{1−X}$FA$_X$PbI$_3$ (FA = formamidinium) PQDs in solar
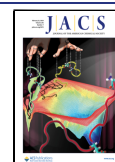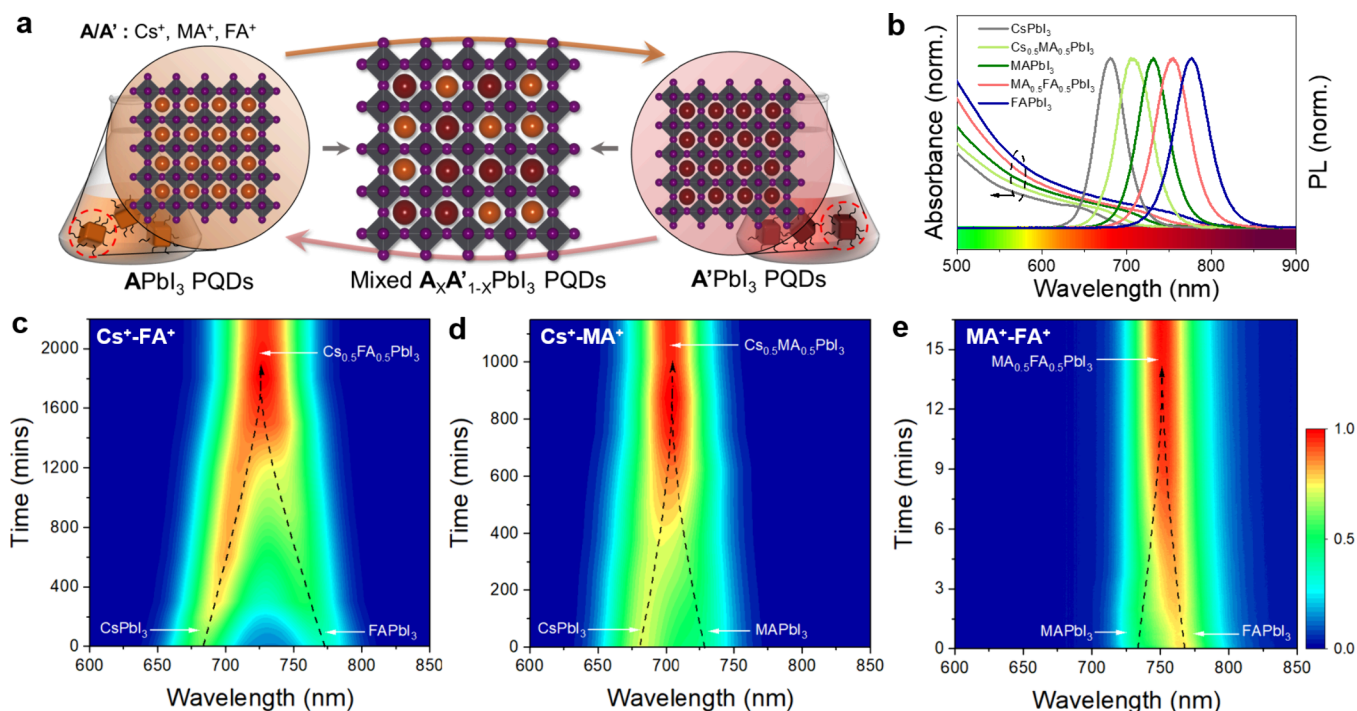
**Figure 1.** (a) Illustration of cation exchange in colloidal PQDs. (b) Absorption and PL spectroscopy of PQDs with different A-site compositions. 2D mapping of PL tracking with time under room temperature for cation exchange reactions of (c) $Cs^+$-$FA^+$, (d) $Cs^+$-$MA^+$, and (e) $MA^+$-$FA^+$.

cells demonstrated an enhanced power conversion efficiency (PCE) exceeding 17%.[27] Nonetheless, unlike halide anion exchange taking place rapidly at room temperature owing to the small activation energy ($E_a$), both the cation exchange process and kinetics are more complicated. The $E_a$ between $Cs^+$ and $FA^+$ cations is measured to be ~0.65 eV,[28] which is higher than the value reported for X-site exchange (~0.45 eV).[29,30] Under these circumstances, a ligand-assisted cation exchange strategy was reported to synthesize high-quality mixed-cation lead triiodide PQDs in a time-efficient manner.[18,27] However, due to the direct mixing of as-synthesized PQDs, the difference in surface ligand conditions, dispersing solvent polarity, and PQD concentration further increases the uncertainty and complexity of such a cation exchange.[31,32] More importantly, additional purification is necessary for removing unreacted precursors, screening the size, and decreasing the ligand density for further device fabrications.

Herein, we reported the cross cation exchange reaction in $MAPbI_3$ and $FAPbI_3$ PQDs, encompassing a time duration within minutes (min), which exhibits almost 2 orders of magnitude faster than widely reported $Cs^+$-$FA^+$ and $Cs^+$-$MA^+$ systems.[28,26] The $E_a$ for $MA^+$-$FA^+$ cross-exchange (~0.35 eV) is measured to show a great reduction relative to the $Cs^+$-$FA^+$ (~0.63 eV) or $Cs^+$-$MA^+$ (~0.57 eV) ones. We proposed a vacancy-assisted cation exchange model and unveiled that the energy barrier associated with the mobility of $MA^+$ and $FA^+$ cations within $MA_{0.5}FA_{0.5}PbI_3$ is notably reduced relative to that of single A-site PQDs, which is mainly due to the changes in the crystal structure and intermolecular interactions. Subsequently, using these mixed-cation PQDs as light absorbance materials, we achieve a champion efficiency of 15.05% for one-step coated PQD solar cells. These mixed PQDs also enable more precisely tunable spectral response in photodetector devices.

## RESULTS AND DISCUSSION

The colloidal lead halide $CsPbI_3$, $MAPbI_3$, and $FAPbI_3$ PQDs in this work were prepared according to reported method with multiple purification processes (Supplementary note 1).[33−35] We first comprehensively characterized the properties of these PQDs by combining UV−visible (UV−vis) absorption spectroscopy (Figure S1), photoluminescence (PL) spectroscopy (Figure S2), Fourier transform infrared spectrometry (FTIR) (Figure S3), and time-resolved PL spectroscopy (TRPL) (Figure S4), evidently demonstrating that we have successfully obtained PQDs with preferred properties and similar low surface ligand density. As shown in Figure 1a, the postsynthetic cation exchange reactions were performed through direct mixing of two different compositions of individual PQD solutions in a controlled proportion to produce the mixed-cation PQDs with tunable spectral absorption and PL from ~680 to ~775 nm (Figure 1b).

We first performed *in situ* PL characterization to monitor the cation exchange between three distinct PQDs with similar conditions at a fixed cation ratio of 1:1. For $Cs^+$-$FA^+$ reaction as depicted in Figure 1c, the distinct PL peak at ~684 nm ($CsPbI_3$ PQD) starts to shift toward longer wavelengths, indicating the expansion of the crystal lattice caused by the alloying of the $FA^+$ cation, and the $FAPbI_3$ peak (~775 nm) shifts toward short wavelengths due to the counter process. The two distinct PL peaks merge into one broad peak after 1200 min, and the full width at half-maximum (fwhm) of the merged PL peak (~730) nm eventually stays constant demanding an extended duration exceeding 2000 min, indicating the formation of stable $Cs_{0.5}FA_{0.5}PbI_3$ PQDs. Similarly, as shown in Figure 1d, the $Cs^+$-$MA^+$ cation exchange reaction takes over roughly 1000 min at room temperature, yielding $Cs_{0.5}MA_{0.5}PbI_3$ PQDs with a PL peak at ~701 nm. In contrast, the $MA^+$-$FA^+$ reaction in Figure 1e remarkably exhibits a fast process within only a few minutes. Upon mixing
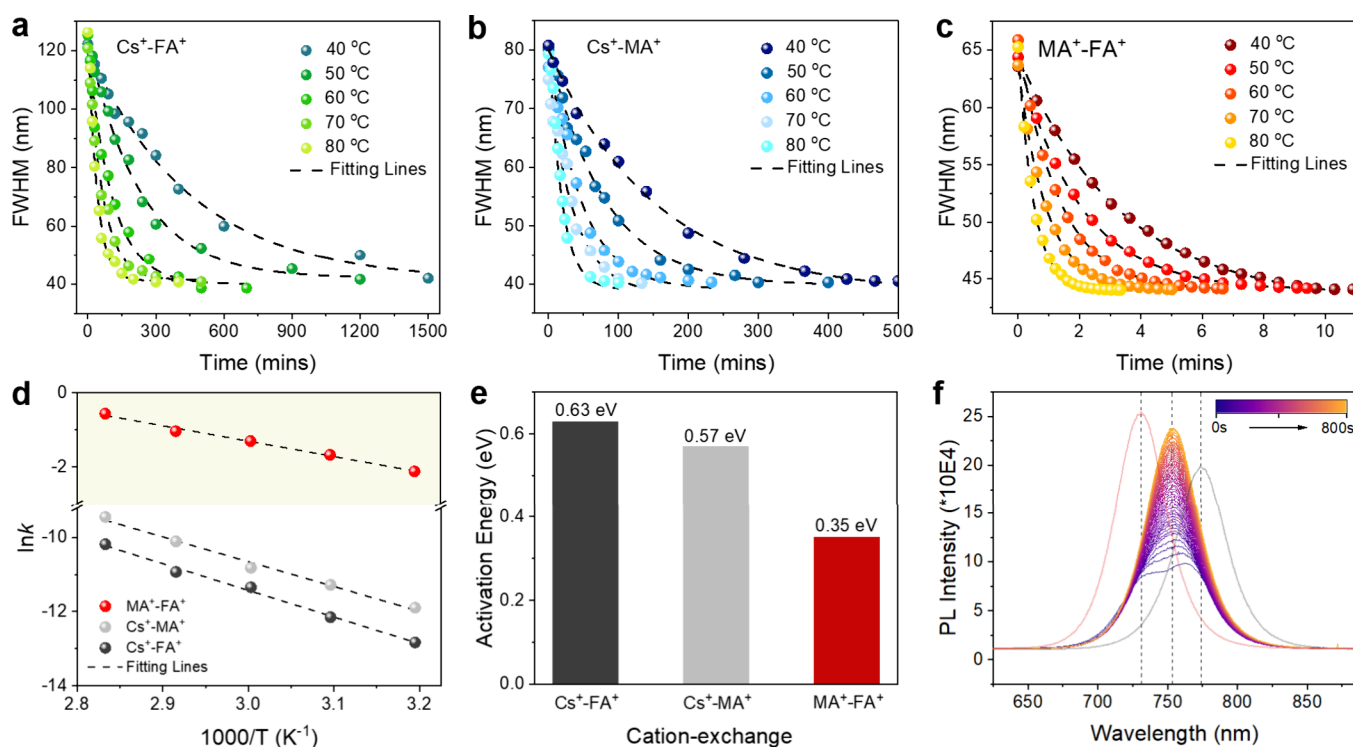
**Figure 2.** FWHM changing with time under 40−80 °C (every 10 °C step) of (a) Cs$^+$-FA$^+$, (b) Cs$^+$-MA$^+$, and (c) MA$^+$-FA$^+$. (d) Arrhenius plots of the fwhm changing rate $k$ with temperature of the above three reactions. (e) Activation energy plots of Cs$^+$-FA$^+$, Cs$^+$-MA$^+$, and MA$^+$-FA$^+$ calculated by the Arrhenius formula. (f) PL evolution of the MA$^+$-FA$^+$ reaction under 40 °C.

MAPbI$_3$ and FAPbI$_3$ PQDs, obvious shifts in the two distinct PL peaks commence instantaneously within seconds and merge into a single broad peak at ~753 nm after 5 min. Over subsequent time, the fwhm of this peak ultimately stabilized at approximately 10 min, indicating the formation of MA$_{0.5}$FA$_{0.5}$PbI$_3$ PQDs. Such a fast exchange process at lower surface ligand conditions is similar to that of halide anion exchange,[29] suggesting a nearly unimpeded energy barrier for the shuttle of rigid cations on the PQD surface and inside lattice. To understand the fast MA$^+$-FA$^+$ exchange, we then performed a cation exchange reaction at varying temperatures to measure the $E_a$ of each reaction. For the Cs$^+$-FA$^+$ exchange, the reaction time duration decreases from 1500 min at 40 °C to 200 min at 80 °C (Figure S5), signifying a faster reaction at an elevated temperature. In addition, we observed the narrowing of fwhm from ~120 to ~42 nm with time shown in Figure 2a, along with the changing rate $k$ that can be obtained by fitting the curves at each temperature. A similar trend can also be observed in Cs$^+$-MA$^+$ exchange, where the reaction time decreases from 500 min at 40 °C to 60 min at 80 °C (Figure S6) and the fwhm narrows from ~80 to ~43 nm (Figure 2b). The fast MA$^+$-FA$^+$ reaction also exhibits a further acceleration at an elevated temperature (Figure S7), and the fwhm narrows from ~65 to ~45 nm (Figure 2c). The $E_a$ of the cation exchange reaction was calculated using the Arrhenius equation, $k = A_0 \exp\left[-\frac{E_a}{k_B T}\right]$. By screening the change in fwhm over time at each temperature and fitting the resultant curves, the reaction rates $k$ with respect to temperature across the above Cs$^+$-MA$^+$, Cs$^+$-FA$^+$, and MA$^+$-FA$^+$ reactions all show a linear trend and can be fitted with a single exponential function in Figure 2d. As depicted in Figure 2e, the $E_a$ of ~0.63 eV associated with the Cs$^+$-FA$^+$ reaction is similar to a previous

report.[28] Meanwhile, the $E_a$ of the Cs$^+$-MA$^+$ reaction slightly decreases to ~0.57 eV, which may be attributed to the smaller ionic radius difference between Cs$^+$ and MA$^+$ cations.[36] Quite unexpectedly, the MA$^+$-FA$^+$ reaction shows a significantly low $E_a$ of ~0.35 eV, which is even lower than that of the reported X-site anion exchange (~0.45 eV).[29] Such a small $E_a$ implies that the time necessary for the MA$^+$-FA$^+$ reaction remains relatively unaffected by temperature fluctuations.

It should be noted that we observed a PL quenching-to-recovering process in the MA$^+$-FA$^+$ system shown in Figure 2f. At the early stage after mixing two PQDs, the PL peaks of both MAPbI$_3$ and FAPbI$_3$ display a significantly quenching process, and the PL peaks gradually increase and eventually stabilize at a subsequent time. Considering the less surface ligand density, the quenching of the PL may be attributed to the formation of the mixed-cation phase at the PQD surface, leading to increased trap states.[37−40] To further understand the concentration effect on the fast cation exchange,[41] we performed an MA$^+$-FA$^+$ exchange reaction under higher concentrations (Figure S8). In the case of 10 mg mL$^{-1}$, we only observe a broad merged PL peak by mixing PQDs, and the whole reaction finished within approximately 300 s. We hypothesized the reaction rate of more free cations and surface vacancies under higher concentrations, increasing collision between PQDs.[32] Furthermore, we extended the exploration to the device-fabrication-scale concentration up to 100 mg mL$^{-1}$, where only a single stable peak at 780 nm can be observed after mixing PQDs, suggesting that postsynthetic cation exchange can efficiently produce the desired composition of PQDs.

Furthermore, first-principles calculations based on density functional theory (DFT) (Supplementary note 2) were carried out to theoretically understand the diffusion of MA$^+$ and FA$^+$ cations inside MAPbI$_3$, FAPbI$_3$, and mixed MA$_{0.5}$FA$_{0.5}$PbI$_3$. In
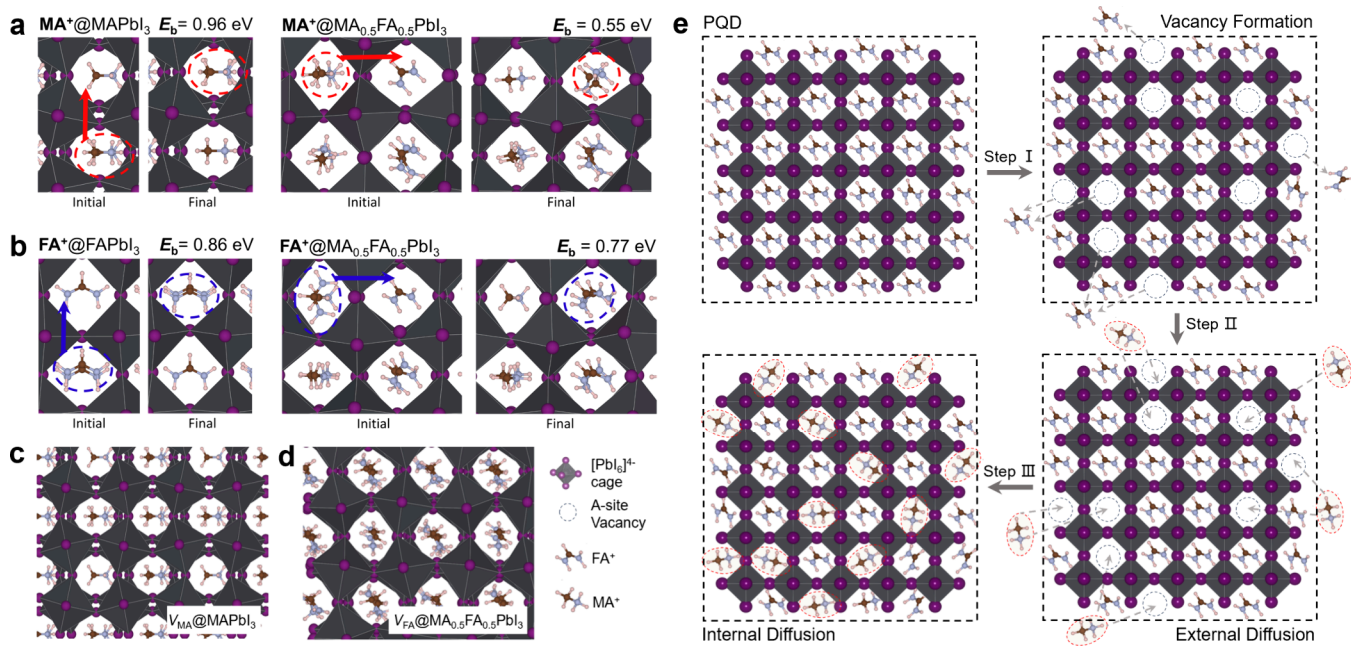
**Figure 3.** (a) DFT simulation of $MA^+$ cation movement in $MAPbI_3$ and $MA_{0.5}FA_{0.5}PbI_3$. (b) DFT simulation of $FA^+$ cation movement in $FAPbI_3$ and $MA_{0.5}FA_{0.5}PbI_3$. Lattice structures of (c) $MAPbI_3$ and (d) $MA_{0.5}FA_{0.5}PbI_3$ with a distorted $[PbI_6]^{4-}$ octahedron. (e) Vacancy-assisted A-site cation diffusion model in a PQD ink solution (the residual ligands are omitted).
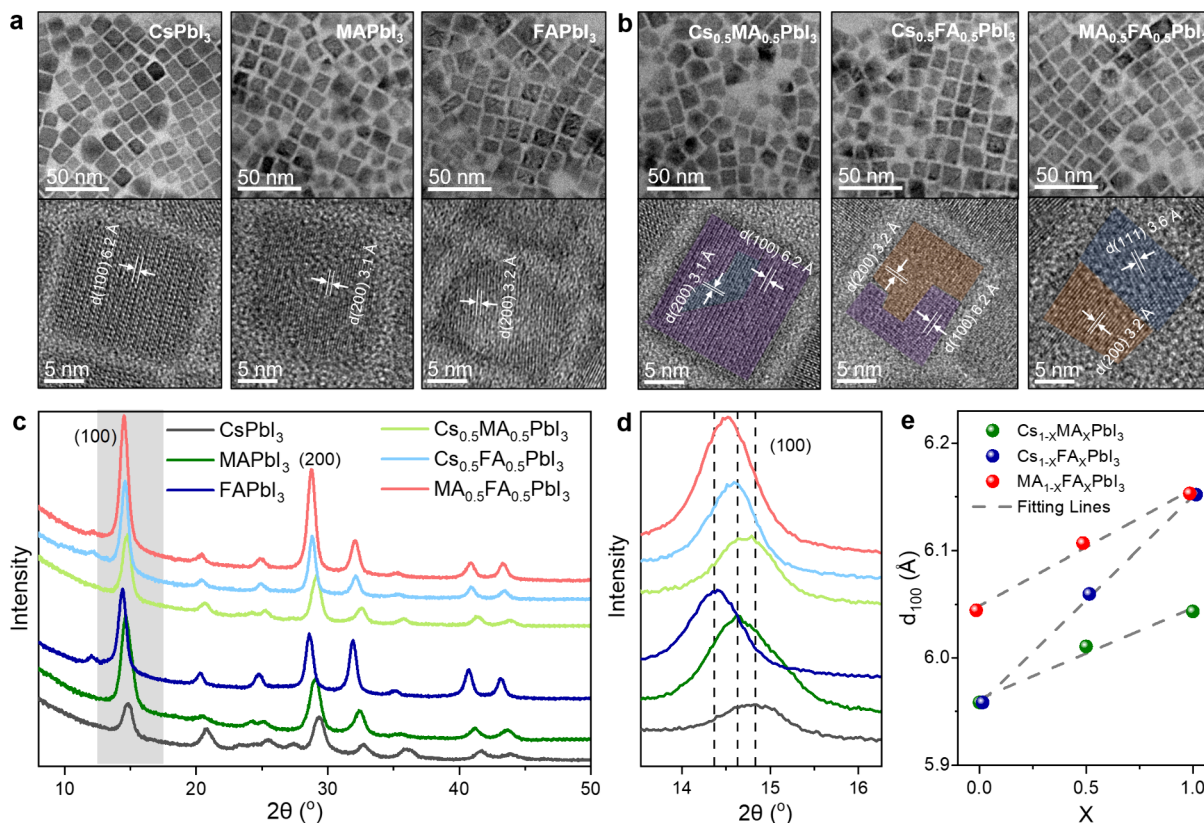


**Figure 4.** Transmission electron microscopy (TEM) images and high-resolution TEM images of (a) $CsPbI_3$, $MAPbI_3$, and $FAPbI_3$. (b) $Cs_{0.5}MA_{0.5}PbI_3$, $Cs_{0.5}FA_{0.5}PbI_3$, and $MA_{0.5}FA_{0.5}PbI_3$. (c,d) X-ray diffraction of different composition PQDs. (e) Linear shift of the $d_{100}$ peak with composition demonstrated by Vegard's law.

both $MA^+$ and $FA^+$ cases, the average cation diffusion energy barriers ($E_b$), estimated for the mixed $MA_{0.5}FA_{0.5}PbI_3$, were smaller than those determined for the corresponding pure systems. For $MA^+$, the $E_b$ in $MAPbI_3$ amounts to 0.96 eV,

whereas in $MA_{0.5}FA_{0.5}PbI_3$, it is 0.55 eV (Figure 3a); that is, a diffusion energy barrier reduction of ~40−50% (extra DFT simulation data shown in Figure S9) to 0.75 eV in $MA_{0.5}FA_{0.5}PbI_3$ (i.e., ~10%, Figure 3b). The $E_b$ reduction in
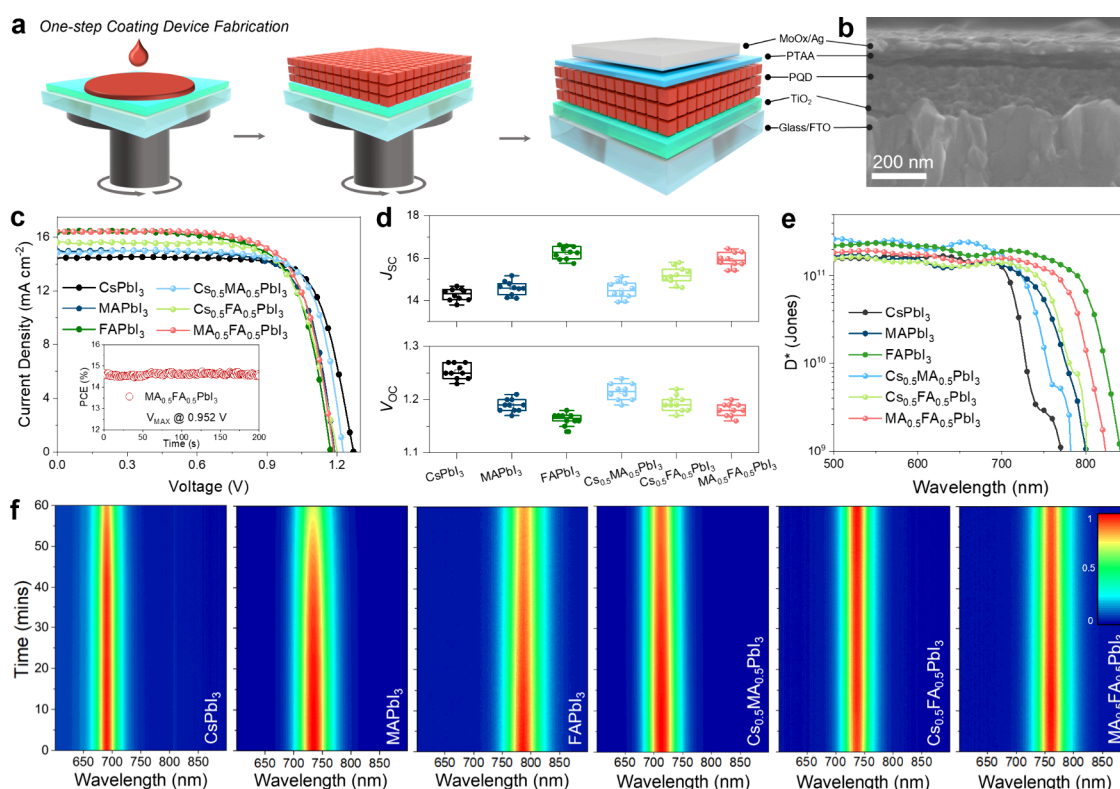
**Figure 5.** (a) Schematic illustration of a one-step PQD deposition for device fabrication. (b) SEM cross-sectional image of the PQD device. (c) $J–V$ curves of PQD solar cells and SPO PCE (inset) of the $MA_{0.5}FA_{0.5}PbI_3$ PQD solar cell. (d) Performance evolution ($J_{SC}$ and $V_{OC}$) of PQD solar cells (10 devices for each composition). (e) Detectivity of PQD photodetectors. (f) *In situ* PL spectra of different PQD films under 100 mW cm$^{-2}$ illumination.

the mixed perovskite structure appears to be related to two main reasons. First, upon creation of organic cation vacancies, the $[PbI_6]^{4-}$ octahedron gets significantly distorted in the pure systems (Figure 3c); however, such $[PbI_6]^{4-}$ distortions are not so pronounced in the mixed perovskite systems (Figure 3d). The $[PbI_6]^{4-}$ octahedron rotations maximize the hydrogen-bond interactions between the I sublattice atoms and H atoms in the organic cations; thus, it gets more difficult for the organic cations to diffuse in the pure perovskites.[42] Second, the middle- and long-range dipole–dipole molecular interactions in the mixed perovskite are significantly disrupted due to the anisotropic mixing of organic cations, thus facilitating the diffusion of molecular cations.[43] Yet, these effects are not present in Cs$^+$ cation exchange reactions. In particular, inorganic Cs$^+$ cations do not possess the characteristics of a dipole, and their small radius leads to a more severe distortion of the $[PbI_6]^{4-}$ octahedron as compared to those in MAPbI$_3$ and FAPbI$_3$. In consequence, the diffusion of Cs$^+$ cations gets hindered in comparison to those of MA$^+$ and FA$^+$.[44]

As depicted in Figure 3e, to fully understand the whole fast MA$^+$-FA$^+$ cation exchange process, we propose a vacancy-assisted cation diffusion model. Considering the less surface ligand density and dynamic surface stabilization in PQDs, surface or near-surface pristine cations will leave the lattice and form sufficient cation vacancies due to the high surface energy and ionic nature of perovskite (step I).[14,45] Moreover, the number of free cations is closely related to the density of surface ligands, the polarity of the solvent, and the concentration of PQDs. Then, by mixing with different PQDs, external cations diffuse along the concentration gradient and occupy the original vacancies to form a mixed-cation phase at or near the PQD surface, which induces stronger PL quenching (step II). Such a diffusion process possesses a lower energy barrier due to the existing sufficient vacancies and large concentration gradient of cations. Finally, after formation of the mixed phase of PQDs, the near-surface cations continue to spread inside the whole crystal lattice assisted by the movement of internal vacancies to achieve a uniform and stable mixed structure (step III). Based on the DFT results, we believe that the final internal diffusion process dominates the rate of the cation exchange reaction.

In the perspective of optoelectronic application, a set of characterizations were performed on the resultant mixed-cation PQDs. Figure 4a depicts TEM images of CsPbI$_3$, MAPbI$_3$, and FAPbI$_3$ PQDs possessing a similar cubic shape with average sizes of ~12.5, ~13.8, and ~16.2 nm, respectively (size distribution shown in Figure S10). The high-resolution TEM (HRTEM) images show a clear lattice arrangement in single PQDs, with a lattice distance of 6.2 Å for the (100) crystal facet of CsPbI$_3$, 3.1 Å for the (200) crystal facet of MAPbI$_3$, and 3.2 Å for the (200) crystal facet of FAPbI$_3$. For the mixed-cation PQDs shown in Figure 4b, they all show similar cubic shapes relative to their single-cation counterparts, confirming that the cation exchange does not have a significant effect on the morphology. In addition, the average size of the mixed-cation PQDs is between the two corresponding single-cation PQDs (shown in Figure S11). For the Cs$^+$-based mixed PQDs, Cs$_{0.5}$MA$_{0.5}$PbI$_3$ and Cs$_{0.5}$FA$_{0.5}$PbI$_3$, they exhibit average sizes of ~12.9 and ~14.7 nm, respectively. The increased size compared to CsPbI$_3$ is attributed to the substitution of Cs$^+$ (~167 pm) with large-sized MA$^+$ (~217 pm) or FA$^+$ (~253

pm). A similar trend was also observed in MA+ and FA+-based mixed PQDs. However, the HRTEM images reveal a local lattice mismatch in all mixed PQDs, suggesting the different cation phase distribution inside a single PQD. In $Cs_{0.5}MA_{0.5}PbI_3$, there are two different lattice arrangements, 6.2 Å corresponding to the (100) crystal facet of $CsPbI_3$ and 3.1 Å corresponding to the (220) crystal facet of $MAPbI_3$. This observation can also be found in other mixed-cation PQDs, indicating a mixed structure on the surface of mixed-cation PQDs.

Furthermore, the bulk structural properties of mixed-cation PQDs were characterized by X-ray diffraction (XRD). As shown in Figure 4c, the mixed-cation PQDs maintain the perovskite crystal structure well with distinct diffraction peaks. For single-cation PQDs, $CsPbI_3$ PQDs show a perovskite $\gamma$-phase (orthorhombic phase), whereas that for $MAPbI_3$ is a $\beta$-phase (tetragonal phase) and for $FAPbI_3$ is the $\alpha$-phase (cubic phase).[46,47] The structure difference between these three PQDs originated from the extent of the corner-shared $[PbI_6]^{4-}$ distortion.[46] The diffraction peaks of Cs+-containing mixed PQDs shift to smaller angles with the incorporation of MA+ or FA+ cations due to their larger size, while those of FA+-containing mixed PQDs shift to the larger angles compared to $FAPbI_3$. Moreover, we further calculated the cation ratio according to the extracted interplanar spacing of the (100) diffraction peak (Figure 4d).[46] As shown in Figure 4e, all of the compositions vary linearly with the presumed compositions, validating our targeted mixed PQDs.

Finally, to explore the benefit of PQDs for device application, the as-prepared mixed-cation PQDs were directly adopted using a one-step coating (Figure 5a) as an active layer for photovoltaic and photodetector applications. In comparison with the widely reported layer-by-layer protocol, these PQDs exhibit a quite uniform surface (Figure S12) and would potentially reduce the energy consumption ratio due to the simplified process. Figure 5b depicts the dual-mode device structure containing glass/fluorine-doped tin oxide (FTO)/ $TiO_2$ (40 nm)/PQDs (~200 nm)/PTAA (60 nm)/$MoO_3$(8 nm)/Ag (120 nm), confirmed by the cross-sectional scanning electron microscopy (SEM) characterizations. The photovoltaic performance was measured under AM 1.5G 100 mW cm$^{-2}$ illumination, with optimal current density−voltage (J−V) curves displayed in Figure 5c and detailed parameters listed in Table S4. In general, the mixed-cation devices all outperform their corresponding single-cation counterparts. The $Cs_{0.5}MA_{0.5}PbI_3$ device exhibits a short-circuit current density ($J_{SC}$) of 14.84 mA cm$^{-2}$, a $V_{OC}$ of 1.21 V, and a fill factor (FF) of 0.77, yielding a PCE of 13.82%. Meanwhile, the $Cs_{0.5}FA_{0.5}PbI_3$ device shows an enhanced $J_{SC}$ of 15.57 mA cm$^{-2}$, a $V_{OC}$ of 1.20 V, and an FF of 0.76, resulting in a higher PCE of 14.20%. In contrast, the fast cation exchange $MA_{0.5}FA_{0.5}PbI_3$ PQD device shows the highest $J_{SC}$ of 16.42 mA cm$^{-2}$ and a $V_{OC}$ of 1.19 V, resulting in a champion PCE of 15.05%, which is the highest reported value for one-step fabricated PQD solar cells.[48,49] The steady-state output (SPO) at the maximum power point shown in Figure 5c exhibits a PCE of 14.6%; in addition, the forward and reverse scan exhibits negligible hysteresis (Figure S13), confirming the reliability of J−V measurements. These enhancements with the use of mixed PQDs can be primarily attributed to the adjustable chemical compositions and lower defect density, which will achieve a well balance between $J_{SC}$ and $V_{OC}$ toward higher PCEs (Figure 5d and Figure S14). The integrated $J_{SC}$

from the external quantum efficiency (EQE) (Figure S15) spectrum further confirms the enhancements in J−V measurement. For the photodetector function, the responsivity spectrum of all devices exhibits a broad detection region from ultraviolet to visible and then to near-infrared (Figure S16). The detectivity ($D^*$) of all of the samples was calculated according to the responsivity and noise signal (Figure S17). As shown in Figure 5e, all devices exhibit similar $D^*$ higher than $10^{11}$ Jones, and the detection can be more precisely tuned from 730 to 810 nm with a tailored composition.

We anticipate that the compositional optimization demonstrated for mixed-cation PQD films would contribute to enhancement of the device stability under illumination. We then investigated the photostability of PQD films by monitoring their PL emission changes before and after continuous light irradiation (400 nm laser with a power density of 100 mW cm$^{-2}$). As shown in Figure 5f, for single-cation PQD films, there was a reduction in PL intensity after 60 min of continuous light irradiation, which may be due to the increased trap states induced by surface ligand shedding.[50] In addition, we observe a blueshift of the PL peak in the $MAPbI_3$ film and a redshift in the $FAPbI_3$ film (1D normalized PL spectra shown in Figure S18). In comparison, for mixed-cation PQD films, we did not observe significant PL intensity reduction after 60 min of continuous irradiation, which may be attributed to the optimal tolerance factors (Table S5) through mixed cations; hence, the phase transition and degradation were suppressed.[51,26] Moreover, there is almost no PL peak shift in the $Cs_{0.5}FA_{0.5}PbI_3$ and $MA_{0.5}FA_{0.5}PbI_3$ PQD films. The enhanced photostability may be attributed to the introduction of larger FA+ cations that improve the lattice stress in the mixed-cation structure, making MA+ cations difficult to remove under illumination.[52]

## ■ CONCLUSIONS

In summary, we investigated the cation exchange reactions between three typical lead triiodide PQDs. The reaction rate of the organic cation (MA+-FA+) was found to be 2 orders of magnitude faster than both Cs+-FA+ or Cs+-MA+. We performed temperature-dependent *in situ* PL characterizations to determine $E_a$ between different cations, and the $E_a$ of MA+-FA+ (~0.35 eV) cross-exchange is measured to show a great reduction relative to Cs+-FA+ (~0.63 eV) or Cs+-MA+ (~0.57 eV). In addition, first-principles calculations suggest that the fast internal cation diffusion arises due to a lowering in structural distortions and the consequent decline in attractive cation−cation and cation−anion interactions in the presence of organic cation vacancies in mixed MA+-FA+ PQDs. Combining these experimental and theoretical evidence, we further proposed a vacancy-assisted cation exchange model to understand the whole process in PQDs with fewer surface ligands. Finally, the prepared mixed-cation PQDs were directly used with a one-step coating process for photovoltaic and photodetector applications, exhibiting a record-high efficiency of 15.05% and more tunable photoresponse, respectively, paving a path toward development of tailored optoelectronic devices.

## ■ EXPERIMENTAL SECTION

**Chemicals.** Cesium carbonate ($Cs_2CO_3$, 99.9%, Sigma), formamidine acetate (FAAc, 99%, Aldrich), methylammonium acetate (MAAc, 99.99%, Greatcell Solar), lead iodide ($PbI_2$, 99.9%, Adamas), oleic acid (OA, 90%, Aldrich), oleylamine (OLA, 90%, Aladdin), 1-

octadecene (1-ODE, 90%, J&K), methyl acetate (MeOAc, anhydrous 99%, J&K), *n*-hexane (anhydrous 97.5%, J&K), *n*-octane (>98%, Alfa Aesar), isopropanol (IPA, 99%, J&k), formamidinium iodide (FAI, 99.99%, Great Solar), toluene (98%, Chinasun Specialty Products Co., Ltd.), titanium tetrachloride (TiCl$_4$, ≥98% purity, Sinopharm Chemical Reagent Co., Ltd.), tris(pentafluorophenyl)borane (95%, Acros Organics), and poly(bis(4-phenyl)(2,4,6-trimethylphenyl) amine) (PTAA, Xi'an Polymer Light Technology Corp.) were utilized. All of these materials were used without further purification. Fluorine-doped tin oxide (FTO) covered glass substrates were purchased from Advanced Election Technology Co., Ltd.

**Preparing Single-Cation PQDs.** CsPbI$_3$, MAPbI$_3$, and FAPbI$_3$ PQDs were synthesized via a hot-injection method as in previous reports.[33−35] For PQDs, the purification steps were as follows: for CsPbI$_3$, the resultant pristine solution of ∼60 mL was added with 240 mL of MeOAc and then centrifuged at 10,000 rpm for 5 min. The precipitate was dispersed in 20 mL of *n*-hexane followed by adding 30 mL of MeOAc with centrifuging at 10,000 rpm for 5 min. The precipitate was dispersed in 1 mL of *n*-octane (∼100 mg mL$^{-1}$) and stored at 5 °C.

For MAPbI$_3$ and FAPbI$_3$, the resultant pristine solution of ∼60 mL was added with 40 mL of MeOAc and then centrifuged at 12,000 rpm for 10 min. The precipitate was dispersed in 20 mL of *n*-hexane followed by adding 40 mL of MeOAc with centrifuging at 12,000 rpm for 10 min. The precipitate was dispersed in 2 mL of *n*-octane (∼100 mg mL$^{-1}$) and stored at 5 °C.

**Preparing Mixed-Cation PQDs.** The mixed-cation PQDs were prepared using a reported postsynthetic cation exchange method by *in situ* PL measurement (Supplementary Figure 18). The concentrations of the PQDs were calibrated by the absorption spectra. As CsPbI$_3$, MAPbI$_3$, and FAPbI$_3$ PQD solutions have similar concentrations, these PQDs were mixed in desired ratios of 1:1 to produce Cs$_{0.5}$MA$_{0.5}$PbI$_3$, Cs$_{0.5}$FA$_{0.5}$PbI$_3$, and MA$_{0.5}$FA$_{0.5}$PbI$_3$ PQDs under room temperature. For the cation exchange kinetic study, these PQDs were kept at a concentration of 1 mg mL$^{-1}$ in *n*-octane and mixed under 40, 50, 60, 70, and 80 °C. For device fabrication, these PQDs were mixed at a concentration of 100 mg mL$^{-1}$ in *n*-octane under room temperature. All of the cation exchange reactions were performed under a sealed environment with slow stirring.

**PQD Device Fabrication.** FTO glass was ultrasonically cleaned with different solvents in the order acetone, dishwashing liquid, acetone, IPA, and acetone, subsequently. Then, after 15 min of ozone, TiO$_2$ of about 50 nm was deposited using TiCl$_4$ on the surface of the FTO by the hydrothermal deposition method. Then, before spinning the PQD layer, the FTO was annealed at 200 °C for half an hour and ozone-treated for 15 min. Varying PQDs (∼100 mg mL$^{-1}$ in *n*-octane), a layer was deposited at 800 rpm for 10 s followed by 2000 rpm for 20 s and then treated by solution of IPA of FAI (1 mg/mL) for 5 s followed by 2000 rpm for 20 s. The film was soaked in IPA of FAI (1 mg/mL) and MeOAc for 5 s, respectively, and then blown dry with N$_2$. A hole transport layer was prepared by mixing 15 mg of PTAA and 15 mg of LAD and 1 mL of toluene. The PTAA solution was then spin-coated on the PQD layer at 3000 rpm for 40 s. MoO$_3$ was deposited at a rate of 0.2 Å s$^{-1}$ for a total thickness of 8 nm. Silver electrodes were evaporated at a rate of 2 Å s$^{-1}$ for a thickness of 120 nm.

## ASSOCIATED CONTENT

### Supporting Information

The Supporting Information is available free of charge at https://pubs.acs.org/doi/10.1021/jacs.3c14000.

> Details of synthesis of PQDs; DFT simulations, UV−vis, FTIR, *in situ* PL and TRPL spectra, TEM and SEM images, *J−V* curves, and solar cell and photodetector device data (PDF)

## AUTHOR INFORMATION

### Corresponding Author

**Jianyu Yuan** − *Institute of Functional Nano & Soft Materials (FUNSOM) and Jiangsu Key Laboratory of Advanced Negative Carbon Technologies, Soochow University, Suzhou, Jiangsu 215123, P. R. China;* orcid.org/0000-0002-5131-1285; Email: jyyuan@suda.edu.cn

### Authors

**Chenyu Zhao** − *Institute of Functional Nano & Soft Materials (FUNSOM) and Jiangsu Key Laboratory of Advanced Negative Carbon Technologies, Soochow University, Suzhou, Jiangsu 215123, P. R. China*

**Claudio Cazorla** − *Departament de Física, Universitat Politècnica de Catalunya, 08034 Barcelona, Spain;* orcid.org/0000-0002-6501-4513

**Xuliang Zhang** − *Institute of Functional Nano & Soft Materials (FUNSOM) and Jiangsu Key Laboratory for Carbon-Based Functional Materials and Devices, Soochow University, Suzhou, Jiangsu 215123, P. R. China*

**Hehe Huang** − *Institute of Functional Nano & Soft Materials (FUNSOM) and Jiangsu Key Laboratory of Advanced Negative Carbon Technologies, Soochow University, Suzhou, Jiangsu 215123, P. R. China*

**Xinyu Zhao** − *Institute of Functional Nano & Soft Materials (FUNSOM) and Jiangsu Key Laboratory of Advanced Negative Carbon Technologies, Soochow University, Suzhou, Jiangsu 215123, P. R. China*

**Du Li** − *Institute of Functional Nano & Soft Materials (FUNSOM) and Jiangsu Key Laboratory of Advanced Negative Carbon Technologies, Soochow University, Suzhou, Jiangsu 215123, P. R. China*

**Junwei Shi** − *Institute of Functional Nano & Soft Materials (FUNSOM), Soochow University, Suzhou, Jiangsu 215123, P. R. China;* orcid.org/0000-0002-0563-6230

**Qian Zhao** − *School of Materials Science and Engineering, Nankai University, Tianjin 300350, P. R. China;* orcid.org/0000-0001-6939-3568

**Wanli Ma** − *Institute of Functional Nano & Soft Materials (FUNSOM) and Jiangsu Key Laboratory for Carbon-Based Functional Materials and Devices, Soochow University, Suzhou, Jiangsu 215123, P. R. China;* orcid.org/0000-0002-2001-3234

Complete contact information is available at:
https://pubs.acs.org/10.1021/jacs.3c14000

### Notes

The authors declare no competing financial interest.

Journal of the American Chemical Society
pubs.acs.org/JACS
Article

## ■ REFERENCES

(1) Swarnkar, A.; Marshall, A. R.; Sanehira, E. M.; Chernomordik, B. D.; Moore, D. T.; Christians, J. A.; Chakrabarti, T.; Luther, J. M. Quantum Dot—Induced Phase Stabilization of $\alpha$-CsPbI$_3$ Perovskite for High-Efficiency Photovoltaics. *Science* 2016, 354 (6308), 92−95.

(2) Chiba, T.; Hayashi, Y.; Ebe, H.; Hoshi, K.; Sato, J.; Sato, S.; Pu, Y.-J.; Ohisa, S.; Kido, J. Anion-Exchange Red Perovskite Quantum Dots with Ammonium Iodine Salts for Highly Efficient Light-Emitting Devices. *Nat. Photonics* 2018, 12 (11), 681−687.

(3) Sanehira, E. M.; Marshall, A. R.; Christians, J. A.; Harvey, S. P.; Ciesielski, P. N.; Wheeler, L. M.; Schulz, P.; Lin, L. Y.; Beard, M. C.; Luther, J. M. Enhanced Mobility CsPbI3 Quantum Dot Arrays for Record-Efficiency, High-Voltage Photovoltaic Cells. *Sci. Adv.* 2017, 3 (10), No. eaao4204.

(4) Protesescu, L.; Yakunin, S.; Bodnarchuk, M. I.; Krieg, F.; Caputo, R.; Hendon, C. H.; Yang, R. X.; Walsh, A.; Kovalenko, M. V. Nanocrystals of Cesium Lead Halide Perovskites (CsPbX3, X = Cl, Br, and I): Novel Optoelectronic Materials Showing Bright Emission with Wide Color Gamut. *Nano Lett.* 2015, 15 (6), 3692−3696.

(5) Huang, H.; Zhang, X.; Gui, R.; Zhao, C.; Guo, J.; Maung, Y. M.; Yin, H.; Ma, W.; Yuan, J. High-Efficiency Perovskite Quantum Dot Photovoltaic with Homogeneous Structure and Energy Landscape. *Adv. Funct. Mater.* 2023, 33 (13), 2210728.

(6) Mei, X.; Wang, J.; Zhang, X.; Zhuang, R.; Hua, Y.; He, K.; Zheng, W.; Zhang, X. In Situ Ligand Compensation of Perovskite Quantum Dots for Efficient Light-Emitting Diodes. *ACS Energy Lett.* 2023, 8 (10), 4386−4396.

(7) Shi, J.; Cohen-Kleinstein, B.; Zhang, X.; Zhao, C.; Zhang, Y.; Ling, X.; Guo, J.; Ko, D.-H.; Xu, B.; Yuan, J.; Ma, W. In Situ Iodide Passivation Toward Efficient CsPbI3 Perovskite Quantum Dot Solar Cells. *NanoMicro Lett.* 2023, 15 (1), 163.

(8) Son, D. H.; Hughes, S. M.; Yin, Y.; Alivisatos, A. P. Cation Exchange Reactions in Ionic Nanocrystals. *Science* 2004, 306 (5698), 1009−1012.

(9) Yuan, J.; Hazarika, A.; Zhao, Q.; Ling, X.; Moot, T.; Ma, W.; Luther, J. M. Metal Halide Perovskites in Quantum Dot Solar Cells: Progress and Prospects. *Joule* 2020, 4 (6), 1160−1185.

(10) Feng, Y.; Ji, Y.; Zhang, Y.; Shao, Q.; Xu, Y.; Li, Y.; Huang, X. Synthesis of Noble Metal Chalcogenides via Cation Exchange Reactions. *Nat. Synth.* 2022, 1 (8), 626−634.

(11) Luther, J. M.; Zheng, H.; Sadtler, B.; Alivisatos, A. P. Synthesis of PbS Nanorods and Other Ionic Nanocrystals of Complex Morphology by Sequential Cation Exchange Reactions. *J. Am. Chem. Soc.* 2009, 131 (46), 16851−16857.

(12) Rivest, J. B.; Jain, P. K. Cation Exchange on the Nanoscale: An Emerging Technique for New Material Synthesis, Device Fabrication, and Chemical Sensing. *Chem. Soc. Rev.* 2013, 42 (1), 89−96.

(13) Nedelcu, G.; Protesescu, L.; Yakunin, S.; Bodnarchuk, M. I.; Grotevent, M. J.; Kovalenko, M. V. Fast Anion-Exchange in Highly Luminescent Nanocrystals of Cesium Lead Halide Perovskites (CsPbX3, X = Cl, Br, I). *Nano Lett.* 2015, 15 (8), 5635−5640.

(14) Scharf, E.; Krieg, F.; Elimelech, O.; Oded, M.; Levi, A.; Dirin, D. N.; Kovalenko, M. V.; Banin, U. Ligands Mediate Anion Exchange between Colloidal Lead-Halide Perovskite Nanocrystals. *Nano Lett.* 2022, 22 (11), 4340−4346.

(15) Zhou, Y.; Fang, T.; Liu, G.; Xiang, H.; Yang, L.; Li, Y.; Wang, R.; Yan, D.; Dong, Y.; Cai, B.; Zeng, H. Perovskite Anion Exchange: A Microdynamics Model and a Polar Adsorption Strategy for Precise Control of Luminescence Color. *Adv. Funct. Mater.* 2021, 31 (51), 2106871.

(16) Haruyama, J.; Sodeyama, K.; Han, L.; Tateyama, Y. First-Principles Study of Ion Diffusion in Perovskite Solar Cell Sensitizers. *J. Am. Chem. Soc.* 2015, 137 (32), 10048−10051.

(17) Takaba, H.; Kimura, S.; Alam, Md. K. Crystal and Electronic Structures of Substituted Halide Perovskites Based on Density Functional Calculation and Molecular Dynamics. *Chem. Phys.* 2017, 485−486, 22−28.

(18) Hao, M.; Bai, Y.; Zeiske, S.; Ren, L.; Liu, J.; Yuan, Y.; Zarrabi, N.; Cheng, N.; Ghasemi, M.; Chen, P.; Lyu, M.; He, D.; Yun, J.-H.; Du, Y.; Wang, Y.; Ding, S.; Armin, A.; Meredith, P.; Liu, G.; Cheng, H.-M.; Wang, L. Ligand-Assisted Cation-Exchange Engineering for High-Efficiency Colloidal Cs1−xFAxPbI3 Quantum Dot Solar Cells with Reduced Phase Segregation. *Nat. Energy.* 2020, 5 (1), 79−88.

(19) Li, H.; Wang, Q.; Oteki, Y.; Ding, C.; Liu, D.; Guo, Y.; Li, Y.; Wei, Y.; Wang, D.; Yang, Y.; Masuda, T.; Chen, M.; Zhang, Z.; Sogabe, T.; Hayase, S.; Okada, Y.; Iikubo, S.; Shen, Q. Enhanced Hot-Phonon Bottleneck Effect on Slowing Hot Carrier Cooling in Metal Halide Perovskite Quantum Dots With Alloyed A-Site. *Adv. Mater.* 2023, 35, 2301834.

(20) Otero-Martínez, C.; Imran, M.; Schrenker, N. J.; Ye, J.; Ji, K.; Rao, A.; Stranks, S. D.; Hoye, R. L. Z.; Bals, S.; Manna, L.; Pérez-Juste, J.; Polavarapu, L. Fast A-Site Cation Cross-Exchange at Room Temperature: Single-to Double- and Triple-Cation Halide Perovskite Nanocrystals. *Angew. Chem., Int. Ed.* 2022, 61 (34), No. e202205617.

(21) Wang, S.; Zhao, Q.; Hazarika, A.; Li, S.; Wu, Y.; Zhai, Y.; Chen, X.; Luther, J. M.; Li, G. Thermal Tolerance of Perovskite Quantum Dots Dependent on A-Site Cation and Surface Ligand. *Nat. Commun.* 2023, 14 (1), 2216.

(22) Li, F.; Zhang, X.; Shi, J.; Jin, L.; Qiao, J.; Guo, J.; Yin, H.; Li, Y.; Yuan, J.; Ma, W. Solution-Mediated Hybrid FAPbI3 Perovskite Quantum Dots for Over 15% Efficient Solar Cell. *Adv. Funct. Mater.* 2023, 33 (40), 2302542.

(23) Zhang, F.; Song, J.; Cai, B.; Chen, X.; Wei, C.; Fang, T.; Zeng, H. Stabilizing Electroluminescence Color of Blue Perovskite LEDs via Amine Group Doping. *Sci. Bull.* 2021, 66 (21), 2189−2198.

(24) Gao, L.; Zhang, Y.; Gou, L.; Wang, Q.; Wang, M.; Zheng, W.; Wang, Y.; Yip, H.-L.; Zhang, J. High Efficiency Pure Blue Perovskite Quantum Dot Light-Emitting Diodes Based on Formamidinium Manipulating Carrier Dynamics and Electron State Filling. *Light. Sci. Appl.* 2022, 11 (1), 346.

(25) Jeong, S.-J.; Cho, S.; Moon, B.; Teku, J. A.; Jeong, M.-H.; Lee, S.; Kim, Y.; Lee, J.-S. Zero Dimensional−Two Dimensional Hybrid Photodetectors Using Multilayer MoS2 and Lead Halide Perovskite Quantum Dots with a Tunable Bandgap. *Acs Appl. Mater. Inter.* 2023, 15 (4), 5432−5438.

(26) Zhang, Y.; Aly, O. F.; De Gorostiza, A.; Shuga Aldeen, T.; Segapeli, A. J.; Korgel, B. A. Cesium Methylammonium Lead Iodide (CsxMA1−xPbI3) Nanocrystals with Wide Range Cation Composition Tuning and Enhanced Thermal Stability of the Perovskite Phase. *Angew. Chem., Int. Ed.* 2023, 62 (31), No. e202306005.

(27) Jia, D.; Chen, J.; Zhuang, R.; Hua, Y.; Zhang, X. Antisolvent-Assisted In Situ Cation Exchange of Perovskite Quantum Dots for Efficient Solar Cells. *Adv. Mater.* 2023, 35 (21), 2212160.

(28) Hazarika, A.; Zhao, Q.; Gaulding, E. A.; Christians, J. A.; Dou, B.; Marshall, A. R.; Moot, T.; Berry, J. J.; Johnson, J. C.; Luther, J. M. Perovskite Quantum Dot Photovoltaic Materials beyond the Reach of Thin Films: Full-Range Tuning of A-Site Cation Composition. *ACS Nano* 2018, 12 (10), 10327−10337.

(29) Koscher, B. A.; Bronstein, N. D.; Olshansky, J. H.; Bekenstein, Y.; Alivisatos, A. P. Surface- vs Diffusion-Limited Mechanisms of Anion Exchange in CsPbBr$_3$ Nanocrystal Cubes Revealed through Kinetic Studies. *J. Am. Chem. Soc.* 2016, 138 (37), 12065−12068.

(30) Pan, D.; Fu, Y.; Chen, J.; Czech, K. J.; Wright, J. C.; Jin, S. Visualization and Studies of Ion-Diffusion Kinetics in Cesium Lead Bromide Perovskite Nanowires. *Nano Lett.* 2018, 18 (3), 1807−1813.

(31) Byranvand, M. M.; Otero-Martínez, C.; Ye, J.; Zuo, W.; Manna, L.; Saliba, M.; Hoye, R. L. Z.; Polavarapu, L. Recent Progress in Mixed A-Site Cation Halide Perovskite Thin-Films and Nanocrystals for Solar Cells and Light-Emitting Diodes. *Adv. Opt. Mater.* 2022, 10 (14), 2200423.

(32) Zhao, C.; Zhang, X.; Huang, H.; Yuan, J. Highly Efficient A-Site Cation Exchange in Perovskite Quantum Dot for Solar Cells. *J. Chem. Phys.* 2022, 157 (3), No. 031101.

(33) Ling, X.; Zhou, S.; Yuan, J.; Shi, J.; Qian, Y.; Larson, B. W.; Zhao, Q.; Qin, C.; Li, F.; Shi, G.; Stewart, C.; Hu, J.; Zhang, X.; Luther, J. M.; Duhm, S.; Ma, W. 14.1% CsPbI3 Perovskite Quantum Dot Solar Cells via Cesium Cation Passivation. *Adv. Energy Mater.* 2019, 9 (28), 1900721.

(34) Huang, H.; Zhao, C.; Zhang, X.; Wang, K.; Fu, J.; Guo, J.; Wang, S.; Zhao, Q.; Ma, W.; Yuan, J. Controllable Colloidal Synthesis of MAPbI3 Perovskite Nanocrystals for Dual-Mode Optoelectronic Applications. *Nano Lett.* **2023**, *23* (19), 9143−9150.

(35) Zhang, X.; Huang, H.; Jin, L.; Wen, C.; Zhao, Q.; Zhao, C.; Guo, J.; Cheng, C.; Wang, H.; Zhang, L.; Li, Y.; Maung Maung, Y.; Yuan, J.; Ma, W. Ligand-Assisted Coupling Manipulation for Efficient and Stable FAPbI3 Colloidal Quantum Dot Solar Cells. *Angew. Chem., Int. Ed.* **2023**, *62* (5), No. e202214241.

(36) Lee, J.-W.; Tan, S.; Seok, S. I.; Yang, Y.; Park, N.-G. Rethinking the A Cation in Halide Perovskites. *Science* **2022**, *375* (6583), No. eabj1186.

(37) Wu, K.; Liang, G.; Shang, Q.; Ren, Y.; Kong, D.; Lian, T. Ultrafast Interfacial Electron and Hole Transfer from CsPbBr3 Perovskite Quantum Dots. *J. Am. Chem. Soc.* **2015**, *137* (40), 12792−12795.

(38) Lim, S.; Lee, G.; Han, S.; Kim, J.; Yun, S.; Lim, J.; Pu, Y.-J.; Ko, M. J.; Park, T.; Choi, J.; Kim, Y. Monodisperse Perovskite Colloidal Quantum Dots Enable High-Efficiency Photovoltaics. *ACS Energy Lett.* **2021**, *6* (6), 2229−2237.

(39) Feng, Q.; Nan, G. How Do A-Site Cations Regulate Trap States at Defective Surfaces of Lead Iodide Perovskites? *J. Phys. Chem. Lett.* **2022**, *13* (21), 4831−4839.

(40) Livakas, N.; Toso, S.; Ivanov, Y. P.; Das, T.; Chakraborty, S.; Divitini, G.; Manna, L.CsPbCl3 → CsPbI3 Exchange in Perovskite Nanocrystals Proceeds through a Jump-the-Gap Reaction Mechanism. *J. Am. Chem. Soc.***2023**. 14520442.

(41) Bilbao, L.; Ortueta, M.; Mijangos, F. Effect of Concentration and Temperature on Mass Transfer in Metal Ion Exchange. *Ind. Eng. Chem. Res.* **2016**, *55* (27), 7287−7295.

(42) Senno, M.; Tinte, S. Mixed Formamidinium−Methylammonium Lead Iodide Perovskite from First-Principles: Hydrogen-Bonding Impact on the Electronic Properties. *Phys. Chem. Chem. Phys.* **2021**, *23* (12), 7376−7385.

(43) Lavén, R.; Koza, M. M.; Malavasi, L.; Perrichon, A.; Appel, M.; Karlsson, M. Rotational Dynamics of Organic Cations in Formamidinium Lead Iodide Perovskites. *J. Phys. Chem. Lett.* **2023**, *14* (11), 2784−2791.

(44) Ghosh, D.; Smith, A. R.; Walker, A. B.; Islam, M. S. Mixed A-Cation Perovskites for Solar Cells: Atomic-Scale Insights Into Structural Distortion, Hydrogen Bonding, and Electronic Properties. *Chem. Mater.* **2018**, *30* (15), 5194−5204.

(45) Akkerman, Q. A.; D'Innocenzo, V.; Accornero, S.; Scarpellini, A.; Petrozza, A.; Prato, M.; Manna, L. Tuning the Optical Properties of Cesium Lead Halide Perovskite Nanocrystals by Anion Exchange Reactions. *J. Am. Chem. Soc.* **2015**, *137* (32), 10276−10281.

(46) Vigil, J. A.; Hazarika, A.; Luther, J. M.; Toney, M. F. FAxCs1−xPbI3 Nanocrystals: Tuning Crystal Symmetry by A-Site Cation Composition. *ACS Energy Lett.* **2020**, *5* (8), 2475−2482.

(47) Zhang, F.; Huang, S.; Wang, P.; Chen, X.; Zhao, S.; Dong, Y.; Zhong, H. Colloidal Synthesis of Air-Stable CH3NH3PbI3 Quantum Dots by Gaining Chemical Insight into the Solvent Effects. *Chem. Mater.* **2017**, *29* (8), 3793−3799.

(48) Kim, J.; Han, S.; Lee, G.; Choi, J.; Jae Ko, M.; Kim, Y. Single-Step-Fabricated Perovskite Quantum Dot Photovoltaic Absorbers Enabled by Surface Ligand Manipulation. *Chem. Eng. J.* **2022**, *448* (15), No. 137672.

(49) Song, H.; Yang, J.; Jeong, W. H.; Lee, J.; Lee, T. H.; Yoon, J. W.; Lee, H.; Ramadan, A. J.; Oliver, R. D. J.; Cho, S. C.; Lim, S. G.; Jang, J. W.; Yu, Z.; Oh, J. T.; Jung, E. D.; Song, M. H.; Park, S. H.; Durrant, J. R.; Snaith, H. J.; Lee, S. U.; Lee, B. R.; Choi, H. A Universal Perovskite Nanocrystal Ink for High-Performance Optoelectronic Devices. *Adv. Mater.* **2023**, *35* (8), 2209486.

(50) An, R.; Zhang, F.; Zou, X.; Tang, Y.; Liang, M.; Oshchapovskyy, I.; Liu, Y.; Honarfar, A.; Zhong, Y.; Li, C.; Geng, H.; Chen, J.; Canton, S. E.; Pullerits, T.; Zheng, K. Photostability and Photodegradation Processes in Colloidal CsPbI3 Perovskite Quantum Dots. *ACS Appl. Mater. Interfaces* **2018**, *10* (45), 39222−39227.

(51) Yang, J.; Hong, Q.; Yuan, Z.; Xu, R.; Guo, X.; Xiong, S.; Liu, X.; Braun, S.; Li, Y.; Tang, J.; Duan, C.; Fahlman, M.; Bao, Q. Unraveling Photostability of Mixed Cation Perovskite Films in Extreme Environment. *Adv. Opt. Mater.* **2018**, *6* (20), 1800262.

(52) Pellet, N.; Gao, P.; Gregori, G.; Yang, T.-Y.; Nazeeruddin, M. K.; Maier, J.; Grätzel, M. Mixed-Organic-Cation Perovskite Photovoltaics for Enhanced Solar-Light Harvesting. *Angew. Chem., Int. Ed.* **2014**, *53* (12), 3151−3157.